

2D Materials-based Electrochemical Triboelectric Nanogenerators

Giuseppina Pace,* Antonio Esau del Rio Castillo, Alessio Lamperti, Simone Lauciello, and Francesco Bonaccorso*

The integration of 2D materials in triboelectric nanogenerators (TENGs) is known to increase the mechanical-to-electrical power conversion efficiency. 2D materials are used in TENGs with multiple roles as triboelectric material, charge-trapping fillers, or as electrodes. Here, novel TENGs based on few-layers graphene (FLG) electrodes and stable gel electrolytes composed of liquid phase exfoliated 2D-transition metal dichalcogenides and polyvinyl alcohol are developed. TENGs embedding FLG and gel composites show competitive open-circuit voltage (≈ 300 V), instant peak power (530 mW m^{-2}), and stability (> 11 months). These values correspond to a seven-fold higher electrical output compared to TENGs embedding bare FLG electrodes. It is demonstrated that such a significant improvement depends on the high electrical double-layer capacitance (EDLC) of FLG electrodes functionalized with the gel composites. The wet encapsulation of the TENGs is shown to be an effective strategy to increase their power output further highlighting the EDLC role. It is also shown that the EDLC is dependent upon the transition metal (W vs Mo) rather than the relative abundance of 1T or 2H phases. Overall, this work lays down the roots for novel sustainable electrochemical-(e)-TENGs developed exploiting strategies typically used in electrochemical capacitors.

1. Introduction

In the last decade, energy harvesters based on mechanical energy conversion have witnessed renewed interest due to the rise of triboelectric nanogenerators (TENGs).^[1–4] Differently from electromagnetic and piezoelectric generators, TENGs can efficiently convert mechanical energy at low force loads and low frequency, while offering sustainable and low-cost production processing.^[5,6] Due to the ubiquitous nature of triboelectrification charging of surfaces, a wide set of triboelectric materials^[7,8] and device configuration^[9] have been tested, demonstrating the large application fields offered by this novel generator, *e.g.*, in wearables,^[10] therapeutics,^[11,12] wind^[13,14] and wave^[15] energy harvesting.

The working principle of TENGs relies on the triboelectrification charging occurring when two materials are placed into physical contact.^[16] The contact-separation mode^[10] is the most common configuration

in which TENGs are operated. In this configuration, the device is constituted of two electrodes and two triboelectric materials (tribomaterial). Each electrode is interfaced with either the electropositive or the electronegative tribomaterial (triboelectrodes). The two triboelectrodes are initially separated by an air gap. During the TENG operation, an external mechanical input takes the two triboelectrodes into intimate contact, allowing the charge transfer between the two tribomaterials.^[17] By connecting the two triboelectrodes to an external electrical circuit, an electrostatic induction occurs and a displacement current is generated according to the Maxwell theory.^[18,19] A following release of the mechanical stress allows for their separation and a current flows through the external circuit.


Strategies so far used to improve TENGs power output include the search for novel, more efficient tribomaterials,^[1,20,7] their nano and micro-structuration to increase the triboelectrification charging,^[21] the use of charge trapping additives,^[22–24] novel electrode engineering^[25,26] and functional interlayers^[27] placed at the interface between the electrode and the tribomaterial. Within this scenario, 2D materials have played a significant role^[28–30] as they can be used as tribomaterials,^[20] charge-trapping additives,^[28] or electrodes as in the case of graphene-based electrodes.^[26]

G. Pace, A. Lamperti
 Institute for Microelectronics and Microsystems – National Research Council (IMM-CNR)

Via C. Olivetti 2, Agrate, Milan 20864, Italy
 E-mail: giuseppina.pace@mdm.imm.cnr.it

G. Pace, S. Lauciello, F. Bonaccorso
 Fondazione Istituto Italiano di Tecnologia (IIT)
 Via Morego, 30, Genova 16136, Italy
 E-mail: f.bonaccorso@bedimensional.it

A. E. del Rio Castillo, F. Bonaccorso
 BeDimensional S.p.A
 Via Lungotorrente Secca 30R, Genova 16163, Italy

 The ORCID identification number(s) for the author(s) of this article can be found under <https://doi.org/10.1002/adma.202211037>

© 2023 The Authors. Advanced Materials published by Wiley-VCH GmbH. This is an open access article under the terms of the Creative Commons Attribution License, which permits use, distribution and reproduction in any medium, provided the original work is properly cited.

DOI: 10.1002/adma.202211037

In our recent work, we highlighted the importance of proper electrode selection and design to improve TENGs performances.^[31] We proposed flexible and all carbon electrodes based on few-layers graphene (FLG) as a sustainable component for the development of wearable, implantable, and biocompatible devices. In another work, we demonstrated the possibility of boosting TENG power output by increasing the electrode quantum capacitance thanks to the introduction of doped graphene in flexible graphene electrodes.^[32] 2D transition metal dichalcogenides (2D-TMDs) are well known to show improved energy storage capabilities compared to traditional electrode materials (e.g., metals) and other 2D materials (e.g., graphene).^[33–35] They can offer several advantages such as large electrochemically active surface area, high surface tunability, rich coordination sites, and both “Faradaic” and “Non-Faradaic” electrochemical behaviours. All these properties make the 2D-TMDs promising high-performing materials in capacitive charging devices, as batteries and supercapacitors, and in capacitive mechanical transducers as TENGs.

A comprehensive summary of the developments made in 2D-material-based TENGs was reported in recent reviews.^[28–30,36,37] A record power output (500 W m^{-2}) was obtained for TENGs based on ferroelectric polymer composites embedding MoS_2 , however, such a high value was reached after electrical pooling of the polymeric film.^[38] High triboelectric performances are also achieved with TENGs integrating M-Xenes, either used as triboelectric material (400 mWm^{-2})^[30] or integrated into polymer-based fiber composites (330 mWm^{-2}).^[39] Different studies have shown high TENGs performances when using MoS_2 composites, showing a power output of a few hundred mW m^{-2} ,^[40,41] and only more recently WS_2 (138 mW m^{-2}).^[42] So far, the observed improvement in TENGs electrical output has mostly been attributed to the intrinsic triboelectric properties of the 2D materials or to their triboelectric charge-trapping capabilities. Here, we study and compare a series of four 2D-TMDs (specifically MoS_2 , WS_2 , WSe_2 , and MoSe_2) integrated into TENGs in the form of polyelectrolyte composite interlayer, a strategy that allowed to reach a peak power output of 530 mW m^{-2} .

In the current work, we provide evidence that the improved performance observed in our TENGs is due to the capacitive charging properties of such 2D materials.

In addition, we demonstrate that the power output of TENGs based on FLG electrodes can be further optimized by increasing their electrochemical double-layer capacitance (EDLC). This is achieved by the introduction of the 2D-TMDs-based polyelectrolyte interlayer placed at the interface between an encapsulating tribomaterial and the FLG-electrode. A seven/fold increase in TENGs power is observed using a polyelectrolyte gel composite based on liquid-phase exfoliated 2D-TMDs, and polyvinyl alcohol (PVA). By investigating the electrochemical performance of supercapacitors embedding the FLG electrodes modified with the gel composite, we provide evidence of the correlation between the TENGs electrical output and the electrode EDLC. The influence of the 1T and 2H phases, commonly found in these 2D-TMDs, on the EDLC is also investigated. Despite previous evidence reporting the higher electrocatalytic activity of the 1T phase compared to the 2H phase, due to a faster electron transfer process occurring at the 1T phase,^[43] we did not observe any specific phase dependence of the TENGs performances. Instead, we

observe higher EDLC and shelf-life stability for W-based chalcogenide TENGs compared to Mo-based ones. The possibility to enhance TENGs power output through the design of efficient EDLC electrodes opens the way to the development of novel sustainable electrochemical-TENGs (e-TENGs) with efficient power output. Such results also mark another essential technological advantage of e-TENGs compared to other mechanical energy harvesters, in particular piezoelectric harvesters, by offering a broader spectrum of device optimization strategies that are drawn on electrochemistry principles.

2. Results and Discussion

2.1. Materials Characterization

The capacitance of liquid phase exfoliated and a few layers 2D-TMDs strongly depends on the size and number of layers of the produced TMDs' flakes. It is reported that a high capacitance in C-based electrodes can be reached if the obtained 2D-TMDs flakes dispersion allows for good electrode wettability and an efficient electrolyte intercalation into the carbon network.^[44] These phenomena would then increase the TMD/electrolyte interface thus enabling a good electronic connection and ensuring a fast charge transfer to the bulk C-electrode.

In this work, few layers thick 2D-TMDs have been produced by liquid phase exfoliation (LPE), in a sustainable solvent (2-propanol), of bulk crystals of WSe_2 ,^[45] WS_2 ,^[46] MoSe_2 ,^[47] and MoS_2 .^[48] The morphological characterization of the exfoliated 2D-TMDs is investigated through Atomic Force Microscopy (AFM). The AFM images (Figure S1, Supporting Information) show the presence of few-layer thick 2D-TMDs flakes with few micrometres lateral sizes, suitable for intercalation and adhesion into the FLG-electrode, thus promoting an efficient charge transfer between the TMDs flakes and the electrode.

Flexible FLG electrodes were prepared from a slurry composed of wet-jet milled graphene, activated carbon, and ethyl-vinyl acetated (EVA) used as binder, according to previously reported method.^[31] The slurry was doctor-bladed onto a sacrificial aluminum foil and subsequently hot-transferred into a flexible EVA substrate to produce a few tens micrometers thick FLG electrode (10–20 μm).

Capacitive, as well as catalytic properties of 2D-TMDs, are often associated with the presence of either the 1T or 2H phase.^[48–50] The 2H phase has a hexagonal lattice with trigonal prismatic metal coordination. It has a semiconducting character, and it is the most favoured thermodynamic phase.^[49] The 1T phase instead, is characterized by octahedral metal coordination with a tetragonal symmetry and a metallic character, which has often been considered at the base of its superior redox activity in catalytic reactions over the 2H phase.^[51] It has also been shown that the exfoliation process induces the phase transition from the naturally found 2H phase to the 1T phase.^[51–55]

The presence of the two phases has been investigated by means of Raman and X-ray photoelectron spectroscopy (XPS) measurements, as reported in **Figure 1** and **2**, respectively.

The 1T phase typically shows a rich Raman spectral signature in the low wavenumber region ($< 300 \text{ cm}^{-1}$). Here, more vibrational modes at lower peak intensities are found compared to the 2H-phase spectra. This evidence is ascribed to the lower symme-

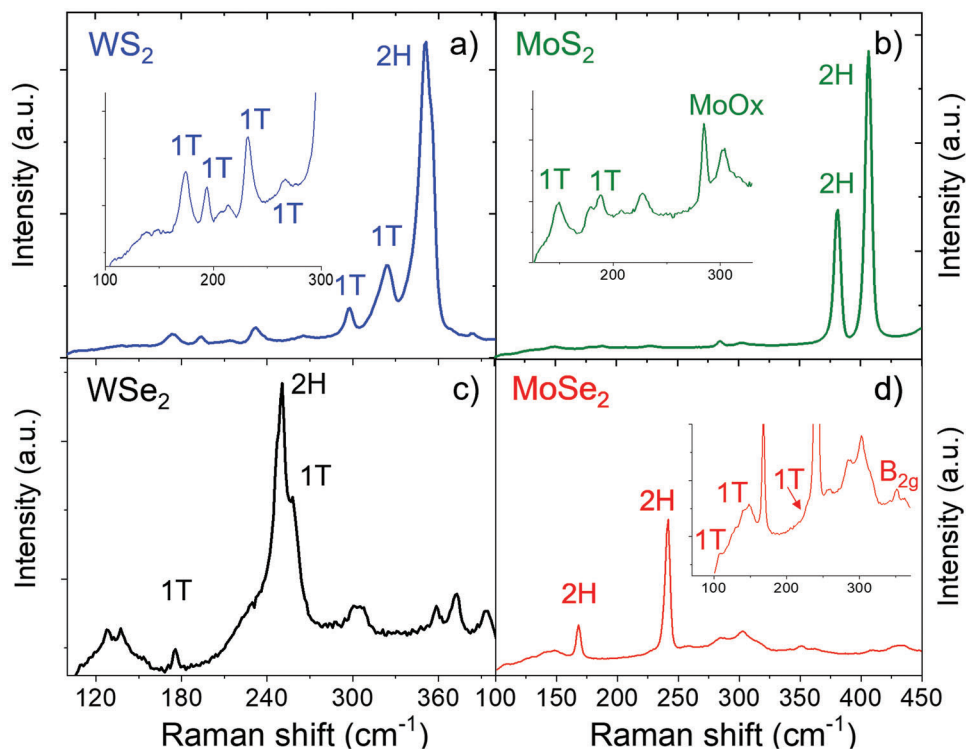


Figure 1. Raman spectra acquired on a) WS_2 , b) MoS_2 , c) WSe_2 , and d) MoSe_2 produced by LPE. Insets show the rich peak distribution observed at low wavenumbers, in which the low intensity 1T phase Raman peaks are typically found.

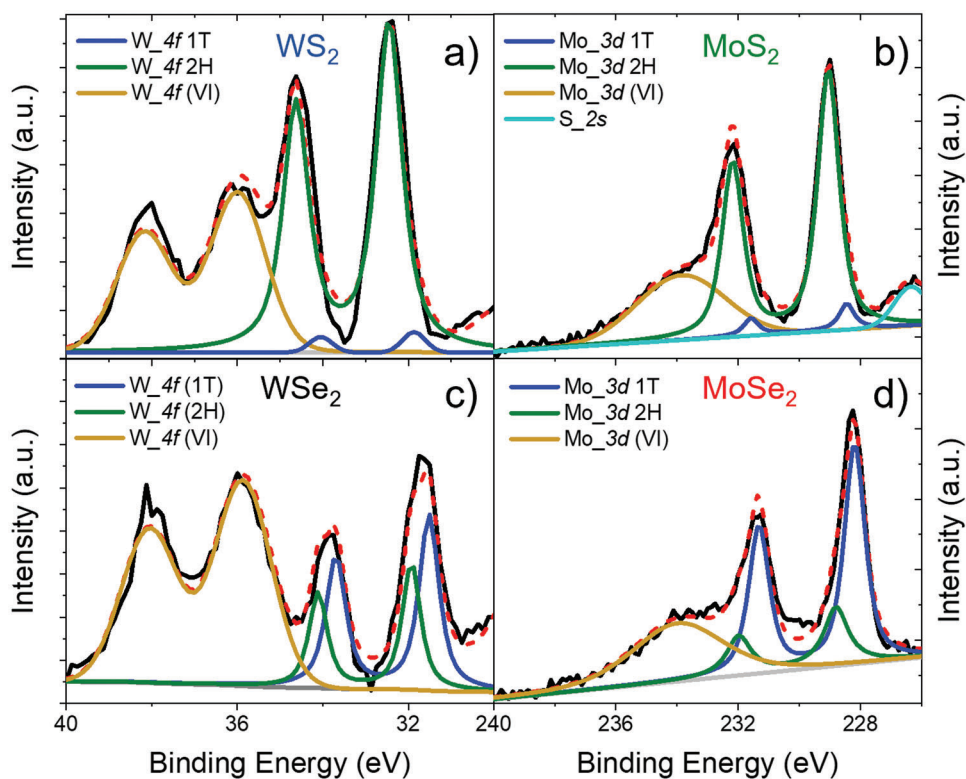


Figure 2. High-resolution XPS spectra of the exfoliated: a) WS_2 (4% 1T); b) MoS_2 (7% 1T); c) WSe_2 (60% 1T); d) MoSe_2 (74% 1T). In all spectra are reported the raw intensity data (black), the background (grey), and the sum spectra of the fitted peaks (red dotted line).

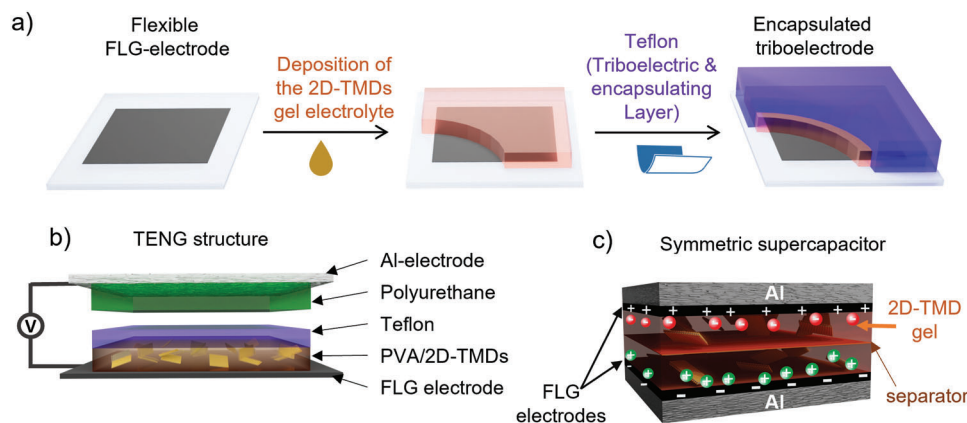


Figure 3. a) Schematic picture of the electronegative triboelectrode fabrication steps. b) Device structure of TENGs investigated in this work and operating in contact-separation mode. c) Device structure of the supercapacitor used for the electrochemical characterization of the 2D-TMDs modified FLG electrodes.

try of the monoclinic 1T phase compared to the hexagonal 2H phase.^[49] A close look at this region (Figure 1, insert), allows identifying the presence of the 1T-modes in all the 2D-TMD samples. Both signature peaks, assigned either to the 1T or 2H phase, can be found in each sample. A detailed assignment of Raman peaks is reported in Figure S4 (Supporting Information).

X-ray photoelectron spectroscopy data confirm the simultaneous presence of the 2H and 1T phases in each 2D-TMD sample. However, they show different relative content per each exfoliated 2D-TMD.

X-ray photoelectron spectroscopy high-resolution spectra of the exfoliated WS₂ and WSe₂ (Figure 2a,c) show the typical W_{4f_{5/2}} and W_{4f_{7/2}} doublet peaks of the chalcogen (30–35 eV), along with the W_{4f} peak of the W(IV) oxide (WO_x) at higher binding energies (35–40 eV)^[56,57] as typically found in exfoliated dispersions.^[45,46,48,58] The deconvolution of the W_{4f} peaks shows the presence of two doublet peaks associated with the 2H (32.45 eV for WS₂; 31.93 eV for WSe₂) and 1T (31.87 eV for WS₂; 31.51 eV for WSe₂) phases.^[49,59] Similarly, high-resolution spectra of MoS₂ and MoSe₂ acquired in the chalcogen binding energy region (226–232 eV) show two pairs of doublets associated with the Mo_{3d_{3/2}} and Mo_{3d_{5/2}}, and assigned respectively to the 2H (229.05 eV for MoS₂; 228.8 eV for MoSe₂) and 1T (228.45 eV for MoS₂; 228.19 for MoSe₂) phases.^[60–62] Signature associated with the Mo(IV) oxide (232–240 eV) is visible in Figure 2b,d. The S_{2s} peak (225.3 eV) is also found in the MoS₂ sample.^[56,63]

The peak analysis of the deconvoluted spectra allows for estimating the relative content of the 2H and 1T phases. Specifically, we found 4% of 1T in WS₂, 60% in WSe₂, 7% in MoS₂, and 74% in MoSe₂. The data show the higher stability of the 1T phase in the Se-based TMDs compared to the sulfur-based ones. The high content of the 1T phase in the selenide-based chalcogenides is also confirmed by the Se_{3d} peak deconvolution (Figure S5, Supporting Information). This finding agrees with Raman's studies (Figure 1) and shows the influence of selenium on the stability of the 1T phase.

It is worth highlighting that the exfoliated 2D-TMDs were used in TENGs and characterized with Raman and XPS measurements after 1 year from their preparation. Furthermore, since the 2H phase mostly characterizes the bulk 2D-TMD crystal, it is ar-

gued that our LPE procedure in 2-propanol may promote the 2H to 1T transition stabilizing the 1T phase.

2.2. TENGs Fabrication and Characterization

Polyvinyl alcohol has been selected to form the gel electrolyte due to its extensive application as an electrolytic medium in supercapacitors, promoting the establishment of an EDLC in carbon-based electrodes.^[64,65] Stable polyelectrolyte gel composites (stability over 2 months stored in vials) are obtained from a dispersion of the exfoliated 2D-TMDs in a PVA gel containing sulfuric acid (H₂SO₄) as electrolyte. The gel composite has then been incorporated as an interlayer between the tribomaterial (Teflon) and the flexible FLG-electrode (Figure 3a). The good dispersion and stability of the 2D-TMDs flakes within the gel enable the uniform adhesion of the PVA composite layer over the entire FLG-electrode surface area as shown by the SEM images (Figure S2, Supporting Information). Teflon is accomplishing a double function of electronegative tribomaterial and encapsulating material allowing water retention in the gel. The final e-TENG device structure is reported in Figure 3b. It contains an electronegative triboelectrode that comprises the FLG electrode, the polyelectrolyte gel composite, the Teflon film and an electropositive triboelectrode formed by a polyurethane (PU) film adhered onto an aluminium foil (FLG/polyelectrolyte-gel/teflon//airgap//PU/Al). The electropositive (PU) and electronegative (Teflon) tribomaterials remained invariant across the different tested TENGs. Therefore, in this device configuration, the performance variation observed across different e-TENGs can be attributed only to the modification of the gel composite interlayer.

Figure 3c presents a schematic of the supercapacitors containing the FLG electrode modified with the gel composite and fabricated following the same procedure applied for the hydrogel functionalized FLG electrodes integrated into the e-TENGs. In the symmetric supercapacitor structure, two FLG-electrodes have been used, respectively as cathode and anodes.

The e-TENGs are operated in contact-separation mode.^[18] High power output (Figure 4) can be obtained when a wet encapsulation is performed, in which the Teflon layer is deposited

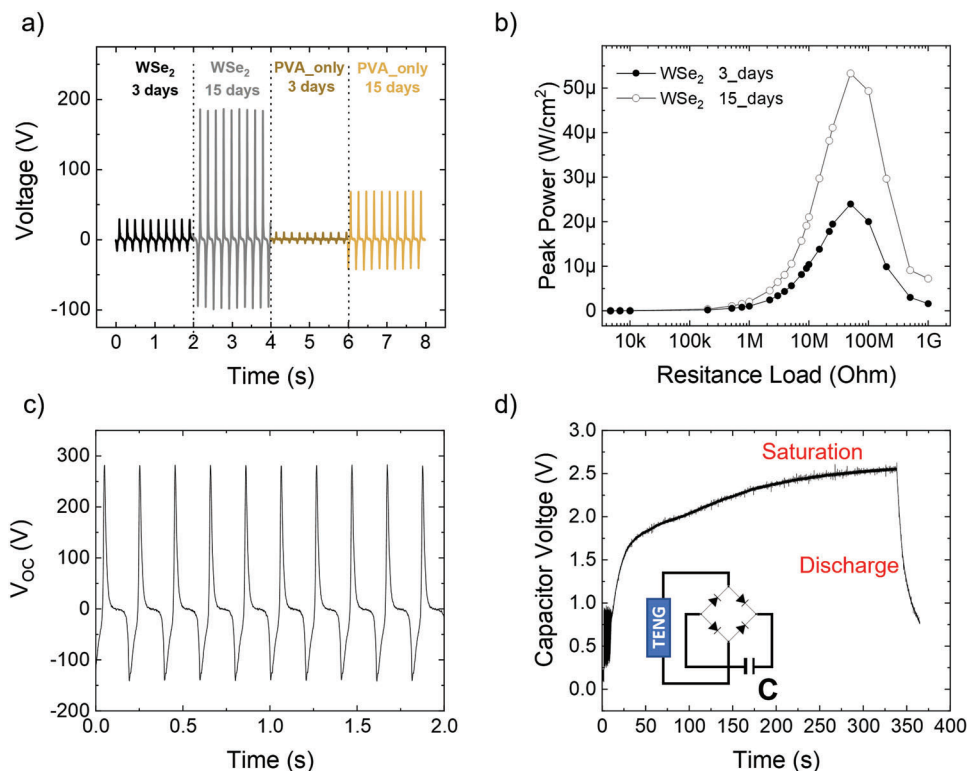


Figure 4. TENG fabricated following the wet encapsulation process with Teflon film. a) TENGs voltage output measured on the day of preparation and after 15 days (10 N, 5 Hz, 40 M Ω , 5 mm airgap, active area 4 \times 4 cm 2). b) Drying time dependence of the instant peak power output measured for TENGs embedding WSe $_2$ gel composites. c) Open Circuit Voltage (V_{OC}) measured for WSe $_2$ -TENG after 15 days of drying, measured with 1 G Ω voltage probe (also Figure S6, Supporting Information). d) The same TENG has been used to charge a 1 μ F capacitor, inset represents the simplified diagram of the electronic circuit used to load the 1 μ F capacitor. (WSe $_2$ -TENG-15days. RMS power 16 μ W cm $^{-2}$ at 5 Hz; PVA only RMS power 2.2 μ W cm $^{-2}$ at 5 Hz).

right after the gel composite deposition on the FLG-electrode. After 15 days, an evident rise in voltage output and instant peak power (Figure 4) is observed, showing the time-dependent electrical performance of the e-TENGs. This time-dependent output is a common feature of all investigated gel-based e-TENGs and is associated with the water content effect on the EDLC formation. In fact, a wet environment allows for greater ionic mobility, thus increasing capacitance and rate diffusion of the electrolyte over the water-wet electrode's surface.^[66,67] Nevertheless, an increased thickness of the interlayer leads to a reduced induction potential at the electrode.^[27] The insertion of the WSe $_2$ gel composite into the e-TENG device structure resulted in more than a 7-fold increase in power output (peak voltage 186 V, peak power 53 μ W cm $^{-2}$, RMS power 16 μ W cm $^{-2}$ at 5 Hz, Figure 4b), compared to the value reached by devices containing only the PVA electrolyte gel (PVA_only devices, 68 V, peak power 7 μ W cm $^{-2}$, RMS power 2 μ W cm $^{-2}$ at 5 Hz, Figure S7, Supporting Information). It is important to highlight that this high-power output, obtained by performing TENG electrode engineering, could be further increased with additional tribomaterial micro- and nanostructuring. For the WSe $_2$ -based TENG, the open circuit voltage (V_{OC}) reached 286 V (Figure 4c) and can effectively be used to store energy in a 1 μ F capacitor (Figure 4d).

However, TENGs fabricated following the wet encapsulation procedure, suffer from gel leakage occurring during the TENGs operation. In fact, under contact pressure, the gel, which is still

wet, tends to escape from the device sides, which are sealed only with paper tape (Figure 4). However, if the encapsulation is performed when the gel is fully dried (Figure S8, Supporting Information), the TENGs performance is rather poor. Furthermore, when the gel electrolyte is left drying overnight in ambient conditions, the gel films deteriorate, with the formation of gel aggregates.

The best compromise, in terms of water retention and time stability, is obtained when the gel is left drying in ambient conditions for 30 min before the encapsulation (data shown in Figure 5, peak power output in Figure S9, Supporting Information). An improved lifetime stability is observed for the W-based TENGs, which retain their electrical output for at least up to 11 months from fabrication (Figure S10, Supporting Information). Contrarily, the Mo-based TENGs show shorter lifetime stability than the other 2D-TMDs. When comparing the e-TENGs voltage output measured after 1 month from fabrication, and after 2 months, we observe a 60% decrease for the MoS $_2$ -based TENGs, a 30% decrease for WS $_2$, 15% for MoSe $_2$, and 4% for WSe $_2$. This evidence shows the superior stability of the W-based TENGs compared to the Mo-based ones, which might reflect the W-based TMDs higher stability toward oxidation.^[68–71] Furthermore, SEM images acquired on films deposited on Al foil, show that during the drying process of the composite film, the WS $_2$ flakes tend to accumulate at the electrode interface (Figure S3, Supporting Information). Such redistribution of the W-based TMDs at the

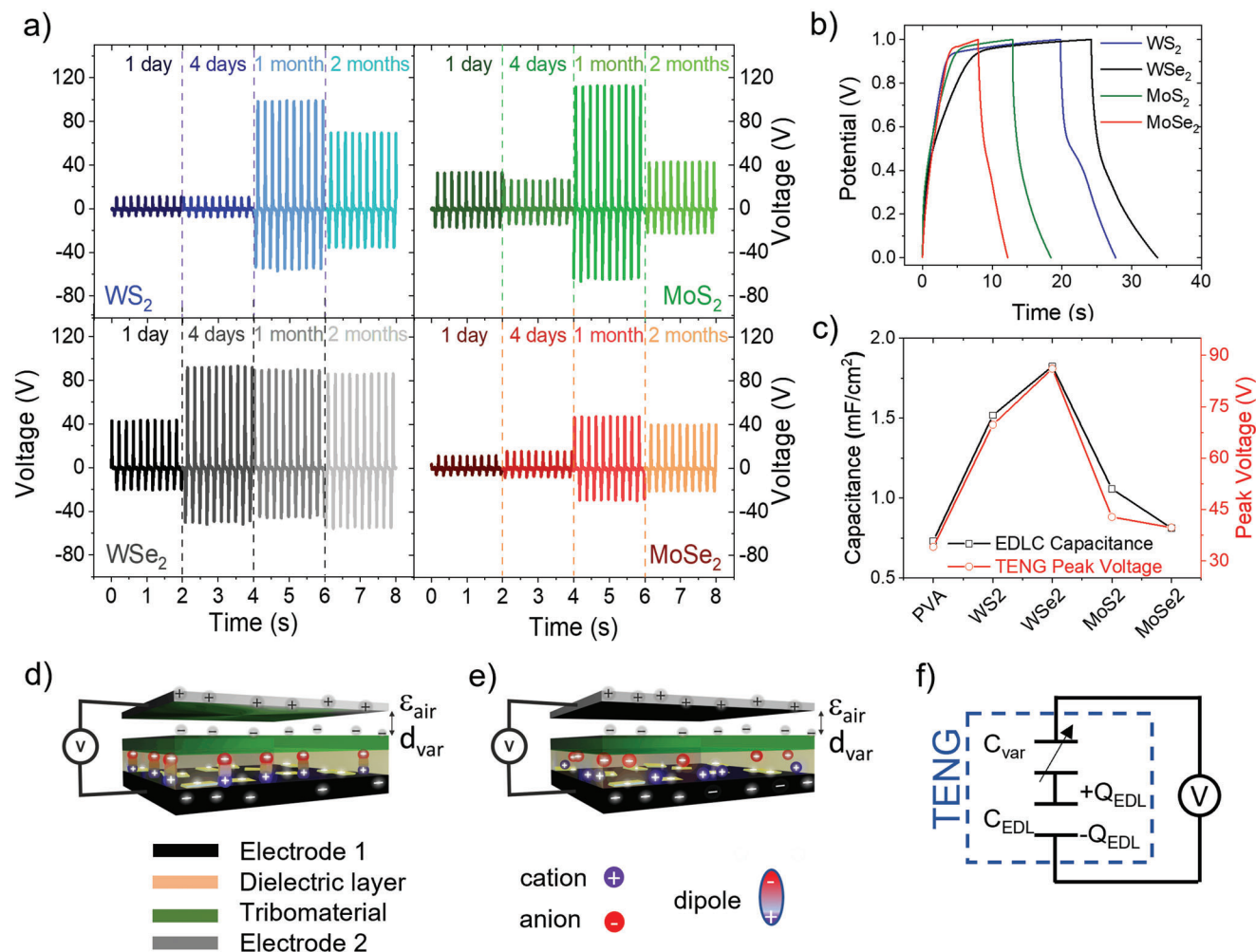


Figure 5. Time-dependent TENG electrical output and correlation with electrochemical performances derived from supercapacitors measurements. a) Time-dependent e-TENGs voltage output. Each train of voltage curves has been measured at different times from the fabrication day (1 day, 4 days, 1 month, 2 months) and under the same operational conditions (10 N, 5 Hz, voltage probe 40 M Ω , airgap 5 mm, \approx 40% humidity, \approx 21 $^{\circ}$ C). b) Galvanostatic charge-discharge curves (set current 150 μ A, set voltage 1 V). c) Correlation between capacitance and peak voltage. Simplified e-TENG structure used to resolve analytically the V_{OC} dependence upon the EDLC: d) scheme of a TENG where only dipole reorientation can occur within the interlayer. e) Scheme of an e-TENG where both dipole reorientation and ionic migration occur after triboelectrification. f) e-TENG equivalent circuit. Electrical double layer capacitance (C_{EDL}), EDL charges (Q_{EDL}), variable capacitance (C_{var}), and variable airgap distance (d_{var}).

interface with the FLG electrodes might improve the FLG/TMD electrical connection (impedance analysis, Figure S15, Supporting Information), thus leading to an increased electrode capacitive charging.

The adoption of the EVA as substrate and Teflon as tribomaterial, known to be excellent moisture- and gas-barrier^[73] contribute to the time stability of the devices. Furthermore, the observed stability of the W-based TENGs (almost 1 year, stored in ambient condition, Figure S10, Supporting Information), can be attributed to the formation of a “quasi” solid-state electrolyte interlayer, which makes our TENGs stable in time despite the non-optimized sealing procedure.

To correlate the e-TENGs electrical performance with the EDLC capacitance of the modified FLG-electrode, current-voltage (Figure S12, Supporting Information) and galvanostatic constant current charge-discharge (GDC) measurements (Figure 5b) were

performed on symmetric supercapacitors comprising the FLG electrodes modified with the gel composite and a glass fiber separator (scheme in Figure 3c). Current-voltage curves reported in the supplementary information (Figure S12, Supporting Information) show a quasi-rectangular shape, as commonly observed in the absence of a pseudocapacitive behavior that would imply the presence of redox reactions.^[74,75] This evidence confirms the double-layer capacitive behavior of the modified FLG-electrodes and the absence of impurities (oxidized flakes) in our wet-jet milled (WJM) graphene, which typically would show pseudo-capacitive behavior.^[76,77]

Galvanostatic charge-discharge measurements (Figure 5b) have been acquired at low specific current (\leq 150 μ A) to approach as much as possible the low current range that is involved in the 2D-TMDs based TENGs operation ($<$ 100 μ A). The capacitance of the 2D-TMDs modified FLG electrodes has been extracted

from the discharge curve of the GDC measurements per each 2D-TMD-based supercapacitor (Figures S12 and S13, Supporting Information). Plotting the discharge curves in logarithmic scale (Figure S12, Supporting Information) highlights the presence of multiple discharge time constants, compatible with multiple discharging mechanisms and consistent with the presence of at least two capacitive materials, the FLG electrode, and the 2D-TMDs.

In particular, the 2D-TMDs-based supercapacitors show an additional discharge time constant, which is instead absent in the PVA_{only} devices and can be associated with the discharging of the TMDs. This feature is clear evidence of the 2D-TMDs contribution to the FLG electrode capacitance.

A correlation is found between the EDLC of the modified FLG-electrode and the relative TENGs electrical performance (Figure 5c). Higher voltage outputs are observed for those 2D-TMDs modified FLG electrodes that show higher EDLC, as found for the WSe₂ and WS₂-based electrodes. This substantial evidence demonstrates how increasing the EDLC of carbon electrodes also determines a boost in TENGs power output.

The model suitable to describe the role of the EDLC in promoting higher power output should consider both the variable capacitance (C_{var}), due to the moving triboelectrode over the airgap distance (d_{var}), and the capacitance of each triboelectrode. To provide an analytical description of the e-TENGs voltage dependence on the EDLC we used the simplified e-TENG structure presented in Figure 5e. In the model architecture, the Al layer is acting both as the electropositive tribomaterial and as electrode, while the second triboelectrode comprises a triboelectric layer and an EDL electrode.^[78] The equivalent circuit related to the simplified e-TENG structure is reported in Figure 5f.

Based on previous models,^[79,80] the maximum voltage reached by the e-TENG can be expressed with the following equation:

$$V_{\text{max}} = \frac{1}{2} V_{\text{TE}} \left(\frac{C_{\text{EDL}}}{C_{\text{min}}} \right) \quad (1)$$

$$V_{\text{TE}} = \frac{Q_{\text{TE}} \cdot d_{\text{TE}}}{A \cdot \epsilon_{\text{TE}}} \quad (2)$$

where C_{EDL} corresponds to the maximum capacitance measured under contact conditions (more details in Supporting Information). C_{min} is the capacitance measured when the two triboelectrodes are placed at their maximum relative distance. V_{TE} is the voltage at the surface of the triboelectric layer and depends on the triboelectric charge distribution (Q_{TE}) over the tribomaterial surface area (A), its permittivity (ϵ_{TE}), and thickness (d_{TE}). In the model, the tribomaterial thickness is assumed to be larger than the gel electrolyte layer thickness. Since the triboelectric layer is the same across all 2D-TENGs, V_{TE} can be considered a constant for all generators, and V_{max} will show a linear dependence on the ratio $C_{\text{EDL}}/C_{\text{min}}$. Therefore, V_{max} is expected to increase with the C_{EDL} . The outcome of Equation. 1 is confirmed by the experimental evidence of the 2D-TENG voltage correlation with the EDLC of the 2D-TMD modified FLG electrode (Figure 5c; Figure S14, Supporting Information).

Figures 5d,e presents a schematic of the different electrode polarization mechanisms that can settle under the establishment of a triboelectrification field in absence (Figure 5d) or presence (Figure 5e) of an electrolytic media. In the case of a non-electrolytic

dielectric, only molecular dipole reorientation can occur (Figure 5d). The addition of an electrolyte to the dielectric layer allows both dipole reorientation and ionic migration, favoring the EDL formation (Figure 5e), thus determining an increased electrode capacitive charging with respect to a non-electrolytic dielectric.

Due to its good conductivity, fast electron-transfer kinetics, and high density of reactive sites (both at the plane edges and basal plane),^[48,50,80] the 1T phase would be expected to favour an increased capacitance of the FLG electrode and therefore, of the TENGs power output. However, despite the significant difference in 1T/2H relative content, as revealed by XPS measurements, no specific correlation is found when we compare the 1T/2H ratio with the trend observed in TENGs power output. Instead, W-based 2D-TMDs provide the most efficient TENGs compared to Mo-based TENGs. The higher stability of W-based TMDs toward oxidation, together with an improved electrical connection to the FLG-electrodes due to interfacial phase segregation, could be the reason for the higher performance and longer lifetime of the W-based TENGs compared to the Mo-based ones. Therefore, the presence of the 1T phase shall not be taken as the foremost responsible for the power output variation observed over the four different 2D-TMDs-based TENGs. A fast charge transfer occurring between the FLG-electrode and the TMDs and the consequent increase in capacitive charging can then be considered responsible for the high capacitance ($\approx 2 \text{ mF cm}^{-2}$) and TENGs power output ($\approx 530 \text{ mW cm}^{-2}$) obtained with the functionalized FLG electrode.

3. Conclusion

The present work introduces a new class of TENGs, the electrochemical-TENGs (e-TENGs), developed following strategies typically used in electrochemistry for enhancing the electrode double-layer capacitance. It is demonstrated that high power output is obtained when the 2D-TMDs-based gel electrolytes are introduced as an interlayer in the TENGs structure, due to the increase of the EDLC of FLG-electrodes. The chemical and structural analysis allows concluding that the observed improvement in TENGs performance is not correlated to the presence of either the 1T or 2H phase typically found in this class of 2D-TMDs. Instead, it is observed that FLG electrodes modified with the W-based 2D-TMDs achieve higher EDLC than the case of Mo-based ones.

Since the substrate (EVA) and triboelectric material (Teflon) are already known to be effective temperature and humidity-resistant, further improvements of this newly designed electrochemical-TENGs are expected if an optimal device sealing is achieved and/or with the choice of alternative electrolytic dielectrics. This further engineering will then allow to widen the application of e-TENGs as stable harvesters and sensors, in fields such as wearables and implantable devices and wave harvesters. In view of these findings, it is important to consider the likelihood, that the increased electrode capacitance due to the addition of 2D nanomaterials might have been overlooked in the literature. The possibility to extend the TENGs design strategies also to include electrochemical parameters, such as electrodes EDLC, will allow to further enhance TENGs output performance, a significant advantage over other mechanical energy harvesters such as piezoelectric and electromagnetic generators.

4. Experimental Section

Production of 2D Materials: Liquid phase exfoliation in 2-propanol of the bulk 2D-TMD crystals was performed as follows: 500 mg of the layered crystals were pestled, thus obtaining powders. Then, the powders were dispersed in 2-propanol, 100 mL, and exfoliated using an ultrasonic bath (Branson 5800 cleaner, Branson Ultrasonics) for six hours.

The obtained dispersions were centrifuged at 2700 g (Rotina) for 60 min at 15 °C. The centrifugation process allowed the sorting of unexfoliated bulk crystals (sediment) from the few layers TMDs in the supernatant. The concentration of the crystals in the supernatant was estimated by drying aliquots of 10 mL and weighing the solid residual. Finally, the concentration of the TMDs dispersions was tuned to 0.2 g L⁻¹ by evaporating the excess solvent.

2D-TMDs Gel Composites Formulation: Poly(vinyl alcohol) (PVA, > 99% hydrolyzed, Mw 146 000–186 000) gel was prepared by dissolving it in water at a concentration of 100 g L⁻¹. The dispersion was placed under vigorous stirring for 30 min. Then the temperature was raised to 85 °C until a clear solution was obtained. PVA gel electrolyte was prepared by dissolving PVA into an acidic water solution containing the H₂SO₄ (50 g L⁻¹), vigorously stirred for 30 min at RT, and subsequently brought to 85 °C until a clear solution was obtained.

The 2D-TMDs gel composites were prepared by mixing the PVA gel with the 2D-TMDs dispersion in the optimized volume ratio of 2:1 (PVA:2D-TMD). The composite gels were placed on a hot plate at 80 °C and under vigorous stirring for 1 h until a clear gel was formed. This formulation allowed the gel composites to remain stable in ambient conditions over weeks, showing the stability of the dispersed 2D-TMDs into the so-formulated electrolyte PVA gel matrix. The reference PVA-only gel was prepared by adding pure 2-propanol in a 2:1 volume ratio. The pH of the obtained gel was tested with a litmus paper and was ~ 1.

All dispersions were heated at 40 °C for 30 min prior to their use. All chemicals were purchased from Merck and used as received.

Production of Few-layers Graphene (FLG): Few-layer graphene flakes were produced via wet-jet-milling (WJM),^[82,83] Briefly, the graphite (20 g L⁻¹) is dispersed in *N*-methyl-2-pyrrolidone, NMP, under high stirring. Briefly, a mixture of the bulk layered crystals (200 g of graphite flakes from Sigma Aldrich) and the solvent (20 L of NMP, Sigma Aldrich) was prepared. The mixture was placed in the container and mixed with a mechanical stirrer (Eurostar digital Ika-Werke). The mixture was processed in the homogenizer, using a nominal pressure of 200 MPa.

Fabrication of Few-layers Graphene (FLG) Electrodes: FLG flakes (WJM), carbon black (Super P, Alfa Aesar), and ethyl vinyl acetate (EVA, Mr Watt Srl) used as a binder at a weight ratio of 1:250:40, were dispersed in a solvent mixture containing butylcarbamate and chlorobenzene (3:7.5 v/v) to form a homogeneous slurry. The slurry was spread on a clean Al foil via doctor blading method, and dried on a hotplate, under ambient conditions, at 100–120 °C for 1 h. The FLG-based film was then transferred onto EVA flexible substrates by hot-pressing the FLG-coated Al film on the EVA substrate (80 °C, 15 min). The Al foil was then peeled off the FLG-coated electrode before use. This resulted in FLG electrodes' thicknesses of 10–20 μm. The electrical connection to external loads was obtained by connecting a copper wire to the FLG electrode with Ag conductive paste.

Materials Characterization: The Atomic force microscopy (AFM) images were acquired with an AFM-Bruker Dimension Edge in tapping mode, using nitrogen-doped silicon cantilevers (PPP-NCHR Nanosensors, USA) with a nominal tip diameter of 10 nm. Gwyddion and Nanoscope Data Processing software were used for image analysis. Scanning Electron Microscopy (SEM) images were acquired with a Field Emission Scanning Electron Microscopy (FE-SEM, Zeiss GeminiSEM 560) operating at 5 kV acceleration voltage and considering secondary electrons.

The XPS characterization was performed with an XPS ESCA 5600 apparatus (monochromatic Al K_α, X-ray source, 1486.6 eV) equipped with a concentric hemispherical analyzer (Physical Electronics Inc., Chanhassen, MN, USA). Pass energy was 58.50 eV with energy steps of 0.25 eV. The binding energy scale was calibrated considering the C 1s peak at 285 eV. XPS spectra analyses were performed using the XPSPEAK41 software and a Voigt shape-fitting function.

Confocal micro-Raman spectroscopy was performed using a Renishaw In-Via spectrometer (New Mills, Kingswood, Wotton-under-Edge, UK) equipped with a solid-state laser source and excitation wavelength of 514 nm (2.41 eV). The laser power was set below 10% of its nominal power (< 1 mW) to avoid sample damage.

Samples for AFM, XPS, and Raman measurements were prepared by drop-casting the 2D-TMDs dispersions onto Si/SiO₂ substrate, followed by drying in ambient conditions.

Gel Composites Electrochemical Characterization: The electrochemical characterization was carried out with a potentiostat/galvanostat (VMP3, Biologic). The electrochemical characterization of the electrolyte gel composites was performed in a symmetric supercapacitor configuration. A Swagelok cell was used for all electrochemical testing. Cyclic voltammetry (CV) measurements were acquired at voltage scan rates ranging from 10 mV s⁻¹ to 200 mV s⁻¹. Galvanostatic charge–discharge (GCD) measurements were carried out at different specific currents, ranging from 150 μA to 2 μA.

The FLG electrodes (1 cm diameter) were cut from the FLG-coated Aluminium (FLG/Al). 500 μl of gel composite was cast on each FLG/Al electrode. A glass fiber membrane (Whatman) was used as an electrode separator.

TENG Fabrication: The 2D TMDs-based gel electrolytes were cast onto the FLG electrode. 1 mL of the gel composites was cast over an electrode area of 4.5 × 4.5 cm². The gel composites were left drying in a controlled atmosphere (humidity 40%, temperature 20–21 °C). The Teflon film (100 μm thick) was placed over the gel to play the function of both triboelectric material and encapsulating film. Sealing was achieved with paper tape, allowing the TENGs shelf-life of a few months. Teflon encapsulation was performed at different timing after drying the gel composite as also reported in Figures 4 and 5 captions. Specifically, in the wet encapsulation, the Teflon layer was placed on top of the polyelectrolyte gel composite soon after the gel deposition on the FLG-electrode.

Though the top and bottom layers were constituted by humidity and gas insulators (EVA as substrate, and Teflon as tribomaterial), the wet encapsulation procedure suffers from gel leakage at the lateral sides of the triboelectrode, which could occur during the e-TENGs operation. To overcome this issue, different strategies were explored to produce optimal e-TENGs with improved lifetime and operational stability. It was observed that when the gel was left to dry overnight before encapsulation with the Teflon layer, only poorly performing e-TENGs were obtained (Figure S11, Supporting Information). Optimal conditions for achieving e-TENGs operational stability and longer lifetime were found when the gel was left drying in ambient conditions for 30 min before the deposition of the Teflon encapsulating film.

TENG Characterization: A home-built set-up was used comprising a linear motor and load cell. The electric measurements were carried out using an oscilloscope (Tektronix MSO5000), a voltage probe 40 MΩ (Tektronix), a current amplifier (1211 DL Instruments), and a home-built resistance commutator for current measurements. Open circuit voltage was measured using a 1 GΩ voltage probe (1000x Tektronix). The device active area was 4 × 4 cm². The device operation parameters were set to an applied force of 10 N, and an operating frequency of 5 Hz. The maximum air gap between the two triboelectrodes was set at 5 mm.

The instant peak power was calculated from the current peak maximum at varying resistance loads ($P = R_{\text{Load}} \times I_{\text{Peak}}^2$). The RMS power was calculated according to the formula $P_{\text{RMS}} = \frac{1}{T} \int_0^T i^2 R dt$, with T being the time interval of an entire cycle at 5 Hz.

A commercial LTC-3588 energy harvester was used to demonstrate the capability of the e-TENGs to charge a storage unit (the LCT-3588 internal capacitor, 1 μF).

Supporting Information

Supporting Information is available from the Wiley Online Library or from the author.

Acknowledgements

Open Access Funding provided by Istituto Italiano di Tecnologia within the CRUI-CARE Agreement.

Conflict of Interest

F.B. is the co-founder, Chief Scientific Officer and Board Member, A.E.D.C. is Senior Scientist at BeDimensional S.p.A., a company that is commercializing 2D materials..

Data Availability Statement

The data that support the findings of this study are available from the corresponding author upon reasonable request.

Keywords

2D materials, electrical double-layers, electrochemical capacitances, flexible electronics, triboelectric nanogenerators

Received: November 26, 2022

Revised: March 12, 2023

Published online:

- [1] Y. S. Choi, S. W. Kim, S. Kar-Narayan, *Adv. Energy Mater.* **2021**, *11*, 2003802.
- [2] Q. Shi, T. He, C. Lee, *Nano Energy* **2019**, *57*, 851.
- [3] X. Cao, Y. Jie, P. Ma, Z. L. Wang, *Nano Energy* **2020**, *78*, 105314.
- [4] J. Chen, Z. L. Wang, *Joule* **2017**, *1*, 480.
- [5] Y. Zi, H. Guo, Z. Wen, M. H. Yeh, C. Hu, Z. L. Wang, *ACS Nano* **2016**, *10*, 4797.
- [6] J. Zhao, G. Zhen, G. Liu, T. Bu, W. Liu, X. Fu, P. Zhang, C. Zhang, Z. L. Wang, *Nano Energy* **2019**, *61*, 111.
- [7] A. Chen, C. Zhang, G. Zhu, Z. L. Wang, *Adv. Sci.* **2020**, *7*, 2000186.
- [8] A. Yu, Y. Zhu, W. Wang, J. Zhai, *Adv. Funct. Mater.* **2019**, *29*, 1900098.
- [9] W. G. Kim, D. W. Kim, I. W. Tcho, J. K. Kim, M. S. Kim, Y. K. Choi, *ACS Nano* **2021**, *15*, 258.
- [10] H. Wang, M. Han, Y. Song, H. Zhang, *Nano Energy* **2021**, *81*, 105627.
- [11] K. Parida, J. Xiong, X. Zhou, P. S. Lee, *Nano Energy* **2019**, *59*, 237.
- [12] G. Conta, A. Libanori, T. Tat, G. Chen, J. Chen, *Adv. Mater.* **2021**, *33*, 2007502.
- [13] Y. Xie, S. Wang, L. Lin, Q. Jing, Z. H. Lin, S. Niu, Z. Wu, Z. L. Wang, *ACS Nano* **2013**, *7*, 7119.
- [14] Z. Ren, L. Wu, Y. Pang, W. Zhang, R. Yang, *Nano Energy* **2022**, *100*, 107522.
- [15] C. Rodrigues, D. Nunes, D. Clemente, N. Mathias, J. M. Correia, P. Rosa-Santos, F. Taveira-Pinto, T. Morais, A. Pereira, J. Ventura, *Energy Environ. Sci.* **2020**, *13*, 2657.
- [16] G. Min, Y. Xu, P. Cochran, N. Gadegaard, D. M. Mulvihill, R. Dahiya, *Nano Energy* **2021**, *83*, 105829.
- [17] W. Xu, M. C. Wong, J. Hao, *Nano Energy* **2019**, *55*, 203.
- [18] Z. L. Wang, *Mater. Today* **2017**, *20*, 74.
- [19] R. D. I. G. Dharmasena, K. D. G. I. Jayawardena, C. A. Mills, J. H. B. Deane, J. V. Anguita, R. A. Dorey, S. R. P. Silva, *Energy Environ. Sci.* **2017**, *10*, 1801.
- [20] M. Seol, S. Kim, Y. Cho, K. E. Byun, H. Kim, J. Kim, S. K. Kim, S. W. Kim, H. J. Shin, S. Park, *Adv. Mater.* **2018**, *30*, 1801210.
- [21] Y. Zou, J. Xu, K. Chen, J. Chen, *Adv. Mater. Technol.* **2021**, *6*, 2000916.
- [22] H. Jiang, H. Lei, Z. Wen, J. Shi, D. Bao, C. Chen, J. Jiang, Q. Guan, X. Sun, S. T. Lee, *Nano Energy* **2020**, *75*, 105011.
- [23] D. W. Kim, J. H. Lee, I. You, J. K. Kim, U. Jeong, *Nano Energy* **2018**, *50*, 192.
- [24] M. Lai, B. Du, H. Guo, Y. Xi, H. Yang, C. Hu, J. Wang, Z. L. Wang, *ACS Appl. Mater. Interf.* **2018**, *10*, 2158.
- [25] D. Yoo, E. Y. Go, D. Choi, J. W. Lee, I. Song, J. Y. Sim, W. Hwang, D. S. Kim, *Nanomaterials* **2019**, *9*, 71.
- [26] L. Shi, S. Dong, P. Ding, J. Chen, S. Liu, S. Huang, H. Xu, U. Farooq, S. Zhang, S. Li, J. Luo, *Nano Energy* **2019**, *55*, 548.
- [27] X. Xie, X. Chen, C. Zhao, Y. Liu, X. Sun, C. Zhao, Z. Wen, *Nano Energy* **2021**, *79*, 105439.
- [28] Y. Liu, J. Ping, Y. Ying, *Adv. Funct. Mater.* **2021**, *31*, 2009994.
- [29] S. A. Han, J. Lee, J. Lin, S. W. Kim, J. H. Kim, *Nano Energy* **2019**, *57*, 680.
- [30] Y. Dong, S. S. K. Mallineni, K. Maleski, H. Behlow, V. N. Mochalin, A. M. Rao, Y. Gogotsi, R. Podila, *Nano Energy* **2018**, *44*, 103.
- [31] G. Pace, A. Ansaldo, M. Serri, S. Lauciello, F. Bonaccorso, *Nano Energy* **2020**, *76*, 104989.
- [32] G. Pace, M. Serri, A. E. del Rio Castillo, A. Ansaldo, S. Lauciello, M. Prato, L. Pasquale, J. Luxa, V. Mazánek, Z. Sofer, F. Bonaccorso, *Nano Energy* **2021**, *87*, 106173.
- [33] Y. Dahiya, M. Hariram, M. Kumar, A. Jain, D. Sarkar, *Coord. Chem. Rev.* **2022**, *451*, 214265.
- [34] L. Lin, W. Lei, S. Zhang, Y. Liu, G. G. Wallace, J. Chen, *Energy Storage Mater.* **2019**, *19*, 408.
- [35] M. A. Bissett, S. D. Worrall, I. A. Kinloch, R. A. W. Dryfe, *Electrochim. Acta* **2016**, *201*, 30.
- [36] M. H. Lee, W. Wu, *Adv. Mater. Technol.* **2022**, *7*, 2101623.
- [37] M. Seol, S. Kim, Y. Cho, K. E. Byun, H. Kim, J. Kim, S. K. Kim, S. W. Kim, H. J. Shin, S. Park, *Adv. Mater.* **2018**, *30*, 1870294.
- [38] M. Kim, D. Park, M. M. Alam, S. Lee, P. Park, J. Nah, *ACS Nano* **2019**, *13*, 4640.
- [39] C. Jiang, C. Wu, X. Li, Y. Yao, L. Lan, F. Zhao, Z. Ye, Y. Ying, J. Ping, *Nano Energy* **2019**, *59*, 268.
- [40] C. Wu, T. W. Kim, J. H. Park, H. An, J. Shao, X. Chen, Z. L. Wang, *ACS Nano* **2017**, *11*, 8356.
- [41] M. Kim, S. H. Kim, M. U. Park, C. J. Lee, M. Kim, Y. Yi, K. H. Yoo, *Nano Energy* **2019**, *65*, 104079.
- [42] T. I. Kim, I. J. Park, S. Kang, T. S. Kim, S. Y. Choi, *ACS Appl. Mater. Interfaces* **2021**, *13*, 21299.
- [43] N. Rohaizad, C. C. Mayorga-Martinez, Z. Sofer, M. Pumera, *ACS Appl. Mater. Interfaces* **2017**, *9*, 40697.
- [44] X. Peng, L. Peng, C. Wu, Y. Xie, *Chem. Soc. Rev.* **2014**, *43*, 3303.
- [45] G. Kakavelakis, A. E. Del Rio Castillo, V. Pellegrini, A. Ansaldo, P. Tzourmpakis, R. Brescia, M. Prato, E. Stratakis, E. Kymakis, F. Bonaccorso, *ACS Nano* **2017**, *11*, 3517.
- [46] S. Bellani, F. Wang, G. Longoni, L. Najafi, R. Oropesa-Nuñez, A. E. Del Rio Castillo, M. Prato, X. Zhuang, V. Pellegrini, X. Feng, F. Bonaccorso, *Nano Lett.* **2018**, *18*, 7155.
- [47] L. Najafi, S. Bellani, R. Oropesa-Nuñez, A. Ansaldo, M. Prato, A. E. Del Rio Castillo, F. Bonaccorso, *Adv. Energy Mater.* **2018**, *8*, 1703212.
- [48] A. Agresti, S. Pescetelli, A. L. Palma, B. Martín-García, L. Najafi, S. Bellani, I. Moreels, M. Prato, F. Bonaccorso, A. Di Carlo, *ACS Energy Lett.* **2019**, *4*, 1862.
- [49] C. C. Mayorga-Martinez, A. Ambrosi, A. Y. S. Eng, Z. Sofer, M. Pumera, *Electrochem. Commun.* **2015**, *56*, 24.
- [50] Z. Lai, Q. He, T. H. Tran, D. V. M. Repaka, D. D. Zhou, Y. Sun, S. Xi, Y. Li, A. Chaturvedi, C. Tan, B. Chen, G. H. Nam, B. Li, C. Ling, W. Zhai, Z. Shi, D. Hu, V. Sharma, Z. Hu, Y. Chen, Z. Zhang, Y. Yu, X. Renshaw Wang, R. V. Ramanujan, Y. Ma, K. Hippalgaonkar, H. Zhang, *Nat. Mater.* **2021**, *20*, 1113.
- [51] D. Voiry, H. Yamaguchi, J. Li, R. Silva, D. C. B. Alves, T. Fujita, M. Chen, T. Asefa, V. B. Shenoy, G. Eda, M. Chhowalla, *Nat. Mater.* **2013**, *12*, 850.
- [52] A. Ambrosi, Z. Sofer, M. Pumera, *Chem. Commun.* **2015**, *51*, 8450.

- [53] D. Voiry, M. Salehi, R. Silva, T. Fujita, M. Chen, T. Asefa, V. B. Shenoy, G. Eda, M. Chhowalla, *Nano Lett.* **2013**, *13*, 6222.
- [54] L. Najafi, S. Bellani, R. Oropesa-Nuñez, A. Ansaldo, M. Prato, A. E. Del Rio Castillo, F. Bonaccorso, *Adv. Energy Mater.* **2018**, *8*, 1801764.
- [55] L. Najafi, S. Bellani, R. Oropesa-Nuñez, B. Martín-García, M. Prato, L. Pasquale, J. K. Panda, P. Marvan, Z. Sofer, F. Bonaccorso, *ACS Catal.* **2020**, *10*, 3313.
- [56] L. Najafi, R. Oropesa-Nunez, S. Bellani, B. Martin-Garcia, L. Pasquale, M. Serri, F. Drago, J. Luxa, Z. Sofer, D. Sedmidubsky, R. Brescia, S. Lauciello, M. I. Zappia, D. V. Shinde, L. Manna, F. Bonaccorso, *ACS Nano* **2022**, *16*, 351.
- [57] A. Katrib, V. Logie, M. Peter, P. Wehrer, L. Hilaire, G. Maire, *J. Chim. Phys. Physico-Chimie Biol.* **1997**, *94*, 1923.
- [58] M. Kang, H. I. Yang, W. Choi, *J Phys D Appl Phys* **2019**, *52*, 505105.
- [59] A. Ambrosi, Z. Sofer, M. Pumera, *Small* **2015**, *11*, 605.
- [60] P. C. Sherrell, P. Palczynski, V. L. Bemmer, C. Mattevi, *Nat. Commun.* **2019**, *10*, 712.
- [61] Y. Yu, G. Nam, Q. He, X. Wu, K. Zhang, Z. Yang, *Nat. Chem.* **2018**, *10*, 638.
- [62] Y. Yin, P. Miao, Y. Zhang, J. Han, X. Zhang, Y. Gong, L. Gu, C. Xu, T. Yao, P. Xu, Y. Wang, B. Song, S. Jin, *Adv. Funct. Mater.* **2017**, *27*, 1606694.
- [63] M. Chen, B. Ji, Z. Dai, X. Du, B. He, G. Chen, D. Liu, S. Chen, K. H. Lo, S. Wang, B. Zhou, H. Pan, *Appl. Surf. Sci.* **2020**, *527*, 146769.
- [64] N. V. Alov, *Phys. Status Solidi Curr. Top. Solid State Phys* **2015**, *12*, 263.
- [65] L. Jiang, X. Lu, *Mater. Chem. Front.* **2021**, *5*, 7479.
- [66] X. Cao, C. Jiang, N. Sun, D. Tan, Q. Li, S. Bi, J. Song, *J. Sci.: Adv. Mater. Devices* **2021**, *6*, 338.
- [67] X. Liu, D. Wu, H. Wang, Q. Wang, *Adv. Mater.* **2014**, *26*, 4370.
- [68] N. C. Osti, B. Dyatkin, M. W. Thompson, F. Tiet, P. Zhang, S. Dai, M. Tyagi, P. T. Cummings, Y. Gogotsi, D. J. Wesolowski, E. Mamontov, *Phys. Rev. Mater.* **2017**, *1*, 065406.
- [69] K. Kang, K. Godin, Y. D. Kim, S. Fu, W. Cha, J. Hone, E. H. Yang, *Adv. Mater.* **2017**, *29*, 1603898.
- [70] L. Gammelgaard, P. R. Whelan, T. J. Booth, P. Bøggild, *Nanoscale* **2021**, *13*, 19238.
- [71] J. Gao, B. Li, J. Tan, P. Chow, T. M. Lu, N. Koratkar, *ACS Nano* **2016**, *10*, 2628.
- [72] J. Martincová, M. Otyepka, P. Lazar, *Chem. – A Eur. J.* **2017**, *23*, 13233.
- [73] F. Corsini, G. Griffini, *JPhys Energy* **2020**, *2*, 031002.
- [74] T. S. Mathis, N. Kurra, X. Wang, D. Pinto, P. Simon, Y. Gogotsi, *Adv. Energy Mater.* **2019**, *9*, 1902007.
- [75] J. Zhao, A. F. Burke, *Adv. Energy Mater.* **2021**, *11*, 2002192.
- [76] M. A. Garakani, S. Bellani, V. Pellegrini, R. Oropesa-Nuñez, A. E. D. R. Castillo, S. Abouali, L. Najafi, B. Martín-García, A. Ansaldo, P. Bondavalli, C. Demirci, V. Romano, E. Mantero, L. Marasco, M. Prato, G. Bracciale, F. Bonaccorso, *Energy Storage Mater.* **2021**, *34*, 1.
- [77] L. Zhang, X. S. Zhao, *Chem. Soc. Rev.* **2009**, *38*, 2520.
- [78] R. Hinchet, A. Ghaffarinejad, Y. Lu, J. Y. Hasani, S. W. Kim, P. Basset, *Nano Energy* **2018**, *47*, 401.
- [79] D. G. Philippe Basset, E. Blokhina, *Electrostatic Kinetic Energy Harvesting*, John Wiley & Sons, Inc., NJ, USA **2016**.
- [80] Y. Zi, S. Niu, J. Wang, Z. Wen, W. Tang, Z. L. Wang, *Nat. Commun.* **2015**, *6*, 8376.
- [81] U. Gupta, B. S. Naidu, U. Maitra, A. Singh, S. N. Shirodkar, U. V. Waghmare, C. N. R. Rao, *APL Mater.* **2014**, *2*, 092802.
- [82] A. E. Del Rio Castillo, V. Pellegrini, A. Ansaldo, F. Ricciardella, H. Sun, L. Marasco, J. Buha, Z. Dang, L. Gagliani, E. Lago, N. Curreli, S. Gentiluomo, F. Palazon, M. Prato, R. Oropesa-Nuñez, P. S. Toth, E. Mantero, M. Crugliano, A. Gamucci, A. Tomadin, M. Polini, F. Bonaccorso, *Mater. Horiz.* **2018**, *5*, 890.
- [83] S. Bellani, E. Petroni, A. E. Del Rio Castillo, N. Curreli, B. Martín-García, R. Oropesa-Nuñez, M. Prato, F. Bonaccorso, *Adv. Funct. Mater.* **2019**, *29*, 1807659.